communications earth & environment

A Nature Portfolio journal

https://doi.org/10.1038/s43247-026-03366-6

Microbial oxidation and carbonate cementation led to three-dimensional preservation of ichthyosaur bones

Check for updates

Andrew Ji Yao Jian[1], **Lorenz Schwark**[2], **Stephen Francis Poropat**[1], **Alex Ian Holman**[1], **Luke Marshall Brosnan**[1], **Maria Diaz Mateus**[1], **Michael Ernst Böttcher**[3,4,5] & **Kliti Grice**[1]

Exceptional preservation of ichthyosaur fossils in the Toarcian (~183–180 Ma) Posidonia Shale of southwest Germany was previously attributed to sustained anoxia or euxinic conditions that excluded aerobic scavengers and promoted early diagenetic mineralization. Here we show a partial ichthyosaur specimen within a carbonate concretion that contained three distinct biogeochemical compartments — the host shale, concretion matrix, and fossil bones — reflecting contrasting redox conditions during decomposition and early diagenesis. Under euxinic conditions, sulfate-reducing bacteria in the sediment generated isotopically light bicarbonate, which precipitated as the micritic calcite of the concretion. The bones uniquely preserve highly degraded, heavy carbon-enriched organic matter and heavy sulfur-enriched barite infilling the marrow cavities. We hypothesize this barite was produced by sulfur-oxidizing bacteria that anaerobically metabolized sulfide to sulfate. These results demonstrate that coupled microbial redox processes and carbonate cementation occurred within microenvironments associated with ichthyosaur bodies that enabled their three-dimensional preservation during the Early Jurassic.

Exceptional preservation of cellular features and biomolecules in the fossil record is rare, as organic remains typically degrade rapidly through scavenging and microbial decomposition[1–3]. Under oxic conditions, efficient recycling reduces the potential for long-term survival of labile organic matter (OM). By contrast, oxygen-depleted (dysoxic to euxinic) environments exclude macro-scavengers and limit decomposition to anaerobic microbes (e.g., bacteria, archaea), which are generally less efficient at decomposing complex OM[4]. These conditions promoted OM accumulation, notably in black shales[5], and sometimes enabled the preservation of soft and skeletal tissues as organic residues without complete mineral replacement[6,7].

While sustained anoxia and reducing conditions are commonly considered essential for exceptional fossil preservation, recent evidence suggests that the interplay between regional environmental redox conditions and microenvironmental redox dynamics may be equally critical[1,8–10]. Oxidative microniches within or surrounding decaying organisms may have enhanced fossilization[7,9–13]. These microniches facilitated partial biomolecular oxidation and early diagenetic mineralization, including carbonate concretion formation[14], which can isolate the remains of organisms from their surroundings, thereby limiting decay and diagenetic deformation[15–17]. The interaction between regional anoxia and microenvironmental oxidation may thus be critical to *Konservat-Lagerstätte* preservation[10–12,18].

The Posidonia Shale of southwest Germany, deposited during the global Toarcian Oceanic Anoxic Event (~183–180 Ma), is an iconic black shale *Konservat-Lagerstätte* renowned for its exceptionally preserved marine palaeofauna[19,20]. Oxygen depletion was linked to basin restriction and water column stratification[5,20–24]. Despite dominantly euxinic bottom waters, geochemical signatures indicate the possible development of benthic oxidative microenvironments, raising questions about the role of chemical gradients associated with redox dynamics in driving exceptional fossil preservation[12].

Here, we report observations from a three-dimensionally (3D) preserved partial ichthyosaur (*Stenopterygius* or *Hauffiopteryx*)[25,26] specimen encased in a carbonate concretion from the Posidonia Shale (Fig. 1) from the Dotternhausen–Dormettingen fossil sites (Baden-Württemberg, Germany; Supplementary Fig. 1). Geochemical and stable isotope analyses of the host shale, the concretion, and the fossil bones reveal a sharp physicochemical gradient between the sulfidic host sediments and the sulfate-enriched bones.

---

[1]Western Australian Organic & Isotope Geochemistry Centre, School of Earth and Planetary Sciences, Curtin University, Perth, WA, Australia. [2]Institute of Geosciences, Christian-Albrechts-University, Kiel, Germany. [3]Geochemistry & Isotope Biogeochemistry, Leibniz-Institute for Baltic Sea Research, Warnemünde, Germany. [4]Marine Geochemistry, University of Greifswald, Greifswald, Germany. [5]Interdisciplinary Faculty, University of Rostock, Rostock, Germany. ✉e-mail: andrew.jian@postgrad.curtin.edu.au; lorenz.schwark@ifg.uni-kiel.de; k.grice@curtin.edu.au

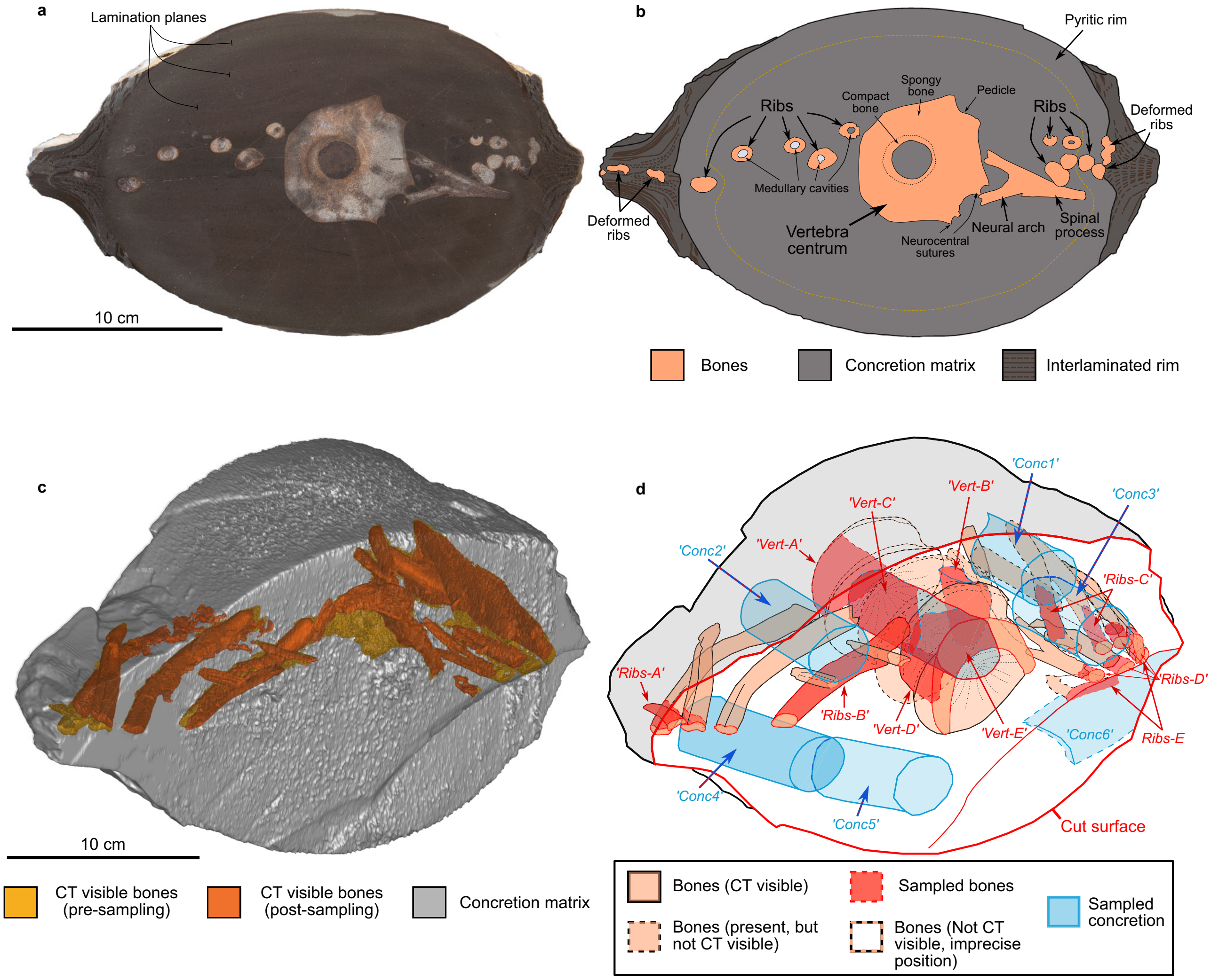

Fig. 1 | Posidonia Shale ichthyosaur specimen within a concretion. **a** Photograph of polished surface, sliced along the transverse plane. Image taken by authors. **b** Schematic annotation of **a** representing skeletal elements and lithological components. Note the deformation of distal ribs in the outer concretion and rim. The rim is composed of calcite cement and shale, indicating concretion growth around the skeleton began in the subsurface. The shale sampled overlaid the concretion and is not shown in the figure. Scale bar for **a–b** 10 cm. **c** 3D isometric view of the sampled concretion section mapped by CT, showing bones before and after destructive sampling. Note anterior vertebral centra and neural spines were present, but not visible on CT due to insufficient density difference, seemingly due to lack of barite. **d** Schematic annotation of **c** indicating sampled vertebrae, ribs, and concretion matrix. Vertebra positions are approximately drawn based on visual identification after the concretion fractured, exposing the vertebral column. Stratigraphic origin of the sample is shown in Supplementary Fig. 1, CT model of the sample prior to destructive sampling shown in Supplementary Fig. 3, sampling process shown in Supplementary Fig. 4, and subsamples shown in Supplementary Fig. 5.

These results offer insights into microbially-mediated oxidative taphonomic pathways during early diagenesis, leading to exceptional fossilization within anoxic and euxinic palaeoenvironments.

Results

Euxinic conditions in sediment and bottom waters

The Posidonia Shale near Dotternhausen–Dormettingen was deposited under dominantly anoxic bottom water conditions, as evidenced by aliphatic biomarker proxies[21,23,24,27] finely laminated bituminous (oil) shales, a lack of bioturbation, abundant framboidal pyrite, and the near absence of benthic fauna in most layers[20,28]. These conditions supported abundant dissimilatory sulfate-reducing bacteria (SRB) in the sediment and bottom water, which produced hydrogen sulfide (H_2S) utilized by phototrophic green sulfur bacteria (GSB, or *Chlorobi*) during anoxygenic photosynthesis, leading to photic zone euxinia (PZE) in the Posidonia Sea[21–23]. The *exaratum* Subzone represents a period of OM-rich accumulation under prolonged PZE at the peak of the Toarcian Carbon Isotope Excursion[21,22]. For the studied specimen, this is confirmed by the presence of GSB carotenoid biomarkers chlorobactane, isorenieratane, and β-isorenieratane in the host shale, concretion, vertebrae, and ribs (Supplementary Fig. 2). Isorenieratane and other isorenieratene-derived compounds are reported from the Posidonia Shale at Holzmaden/Ohmden and the age-equivalent Bächental oil shales within the Middle Allgäu Formation (Austria)[29], indicating broad extent of PZE in the SW German Basin.

Shale and Concretion

The host shale surrounding the concretion contains approximately 9.6 wt.% total organic carbon (TOC) (Table 1), shows a high hydrogen index (HI = 675 mg HC/g TOC), low oxygen index (OI = 8 mg CO_2/g TOC), and a relatively low T_{max} of 420 °C, all indicating excellent OM preservation and low thermal maturity (Fig. 2a, b). The concretion rim — composed of interlaminated shale and carbonate cement (Fig. 1a, b) — has comparable HI (559 mg HC/g TOC), OI (15 mg CO_2/g TOC), and T_{max} (426 °C) values to those of the host shale (Fig. 2a, b).

Carbonate concretions are common in the Posidonia Shale[30], with particularly high abundance in the *exaratum* Subzone. Their formation was

Table 1 | HAWK programmed pyrolysis (Rock Eval) data

Sample	S1 (mg HC/ g rock)	S2 (mg HC/ g rock)	TOC (% wt.)	Tmax (°C)	HI (mg HC/ g TOC)	OI (mg CO_2/ g TOC)
Vert-A	0.01	0.7	0.8	448	87	120
Vert-B	0.01	0.6	0.9	449	72	115
Vert-C	0.04	0.7	0.8	448	81	78
Vert-D	0.00	0.4	0.7	447	56	103
Vert-E	0.02	0.3	0.8	448	42	68
Vertebrae $\bar{x}$ ($n = 5$)	0.02	0.6	0.8	448	68	97
Ribs-A	0.05	8.6	2.0	435	393	74
Ribs-B	0.02	1.1	0.9	442	130	99
Ribs-C	0.03	1.4	1.1	445	125	80
Ribs-D	0.02	2.1	1.1	440	190	107
Ribs-E	0.02	2.3	1.5	436	154	36
Ribs $\bar{x}$ ($n = 5$)	0.03	3.1	1.3	440	198	79
Conc1-A	0.05	3.2	1.2	431	279	54
Conc1-B	0.06	3.1	1.3	431	247	62
Conc2-A	0.04	2.5	1.1	429	226	44
Conc2-B	0.04	2.8	1.0	430	270	57
Conc2-C	0.06	2.5	1.3	431	192	51
Conc3-A	0.04	2.0	1.2	431	172	48
Conc3-B	0.03	2.3	1.0	432	219	62
Conc4-A	0.06	3.7	1.3	430	278	46
Conc4-B	0.04	3.3	1.1	430	290	37
Conc4-C	0.04	3.1	1.1	432	284	61
Conc5-A	0.08	3.8	1.2	430	316	38
Conc5-B	0.05	4.3	1.2	430	361	43
Conc5-C	0.05	3.1	1.3	432	241	56
Conc6	0.04	3.0	1.3	430	242	43
Concretion $\bar{x}$ ($n = 14$)	0.05	3.0	1.2	431	258	50
Rim	0.04	20.9	3.7	426	559	15
Shale	0.11	64.5	9.5	420	675	8
Rim/Shale $\bar{x}$ ($n = 2$)	0.07	42.7	6.6	423	617	12

Values for each sample represent the average of triplicate runs. Component averages ($\bar{x}$) and sample sizes indicated.

microbially mediated by SRB, which produced bicarbonate (Equations 1, 2)[14] that subsequently precipitated as micritic calcite (Equation 3) around a nucleus, which occasionally was a fossil[30,31]. Only ~10–20% of Dotternhausen–Dormettingen concretions contain a fossil[32], sometimes including marine reptile remains. However, concretionary ichthyosaur specimens are often incomplete as their large size often precluded complete encapsulation[31,33,34].

The encapsulating concretion matrix shows a marked dilution of OM due to carbonate formation, with TOC declining to 1.2% (Table 1). Compositional changes in OM were unaffected by carbonate dilution but reflect preferential degradation of labile OM with HI decreasing to 268 mg HC/g TOC, OI increasing to 51 mg CO_2/g TOC, and T_{max} increasing to 430 °C, the latter being indicative of the preservation of a more recalcitrant fraction of the original OM (Fig. 2a, b).

The concretion carbonate is depleted in ^{13}C ($\delta^{13}C_{carb}$ $\bar{x} = -13.7 \pm 2.1$ ‰ VPDB) compared to the host shale, indicating calcite precipitation from a solution containing bicarbonate from microbial OM remineralisation[30].

The concretion also contrasts with the shale and the fossil bones in showing relatively ^{18}O-enriched oxygen isotope values ($\bar{x}$ -3.9 ± 0.6 ‰ VPDB) (Fig. 2e), suggesting a different composition of the concretion-forming fluid compared with those precipitating solids in the surrounding reservoirs[35].

The total sulfur $\delta^{34}S$ values increase from -18.8 ± 0.6 ‰ in the shale, to -10.4 ± 1.5 ‰ (VCDT) in the concretion, consistent with progressive net microbial sulfate reduction[36] (Fig. 2f). The host shale deposited under euxinic conditions contains only reduced S species, while the concretion on average contains 12 times more reduced than oxidized S species (Table 2). Total reduced inorganic sulfur (TRIS) $\delta^{34}S$ values of the concretion increase by an average of ~7.9 ‰ from the shale (Table 2), indicating greater SRB activity fractionating isotopically light sulfur and leaving behind isotopically heavy framboidal pyrite (Supplementary Fig. 7)[36,37]. Although $\delta^{34}S$ variability within the concretion is limited, higher total S concentrations positively correlate with a minor ^{34}S enrichment (Supplementary Fig. 8a). Concretion TRIS concentrations also correlate with $\delta^{34}S_{TRIS}$ enrichment (Supplementary Fig. 8b). The $\delta^{15}N_{total}$ values rise from +2.5 ‰ in the shale, to $+4.8 \pm 0.7$ ‰ in the concretion (Table 2), reflecting either preferential loss of ^{14}N from sediment organic nitrogen or an increase in alkalinity that facilitated carbonate precipitation[38].

Fossil Bones

The bones differ markedly in the degree of OM preservation compared to both the shale and the concretion, as indicated by stippled lines in Fig. 2a, f that separate the bone samples from the concretion and shale. The vertebrae contain lower TOC ($\bar{x} = 0.82$ %) than the ribs ($\bar{x} = 1.32$ %) (Table. 1), with correspondingly lower average HI (68 *vs.* 198 mg HC/g TOC) and higher average OI (97 *vs.* 79 mg CO_2/g TOC), indicating more advanced OM degradation in the vertebrae (Fig. 2a, b). T_{max} values are higher in vertebrae (448 °C) than in ribs (440 °C), reflecting greater alteration and the dominance of recalcitrant OM.

The $\delta^{13}C_{org}$ values of the bones (vertebrae $\bar{x} = -31.1 \pm 0.5$ ‰, ribs $\bar{x} = -31.7 \pm 0.5$ ‰) are enriched by ~1.6 ‰ relative to the concretion and shale (Fig. 2c, d; Table 1), indicating preferential microbial metabolism of ^{12}C compared to the sediment biomass. The relatively enhanced $\delta^{15}N_{total}$ values of the bones (vertebrae $\bar{x} = +3.4 \pm 1.0$ ‰; ribs $\bar{x} = +2.9 \pm 1.1$ ‰) are more comparable to those of the concretion ($+4.8 \pm 0.7$ ‰) than the shale (+2.5 ‰), indicative of microbial ^{14}N removal (Table 2).

Total sulfur isotope measurements show strong ^{34}S enrichment in bones (ribs $\bar{x} = +13.8 \pm 2.0$ ‰, vertebrae $\bar{x} = +7.3 \pm 4.0$ ‰), distinct from sediment and concretion. Trace amounts of TRIS were detected in vertebrae (0.04 wt.%) and ribs (0.3 wt.%) while dominant $S_{sulfate}$ is 2.5 and 10.0 wt.%, respectively (Table 2). The $\delta^{34}S_{TRIS}$ values of the bones are depleted (ribs $\bar{x} = -10.3 \pm 2.6$‰; vertebrae $\bar{x} = -7.3 \pm 1.2$‰), like the concretion, in which TRIS (3.7 wt. %) dominates over $S_{sulfate}$ (0.8 wt. %). Dissolved sulfate enriched in ^{34}S was present during carcass decomposition and fixed in bones (Fig. 2f)[39], with the ribs containing $\delta^{34}S_{sulfate}$ average values of $+14.5 \pm 1.8$ ‰ and vertebrae average values of $+11.4 \pm 1.0$ (Table 2). The ^{34}S-enrichment also correlates with higher total S concentrations (Supplementary Fig. 8a).

OM and stable isotope signatures within the bones are spatially variable within the concretion, indicating a gradient in bone OM degradation. Distal rib sections (Ribs-A, E, Fig. 1d) exhibit higher HI and lower OI, whereas the innermost rib sections (Ribs-B, C, D, Fig. 1d) show relatively enriched bulk $\delta^{13}C_{org}$ values (Fig. 2c, d). Vertebra samples (Fig. 1) contain the most hydrogen-depleted and most enriched $\delta^{13}C_{org}$ values (Fig. 2c). The $\delta^{13}C_{carb}$ and $\delta^{18}O_{carb}$ values of the bones are consistent with low-temperature diagenesis under anoxic conditions (Fig. 2e) and show a distinct separation between proximal and distal bone sections (Fig. 2d, e), likely reflective of spatiotemporal chemical shifts during concretion nucleation.

Micro-phase mineralogical analyses reveal a complex alteration sequence associated with diagenetic structure development. Calcite ($CaCO_3$) and sparry barite ($BaSO_4$) infilled the marrow cavities (Fig. 3a, i), while the original bone collagen and hydroxyapatite ($Ca_5[PO_4]_3OH$) recrystallized to fluorapatite ($Ca_5[PO_4]_3F$) (Figs. 3c–m, 4). The

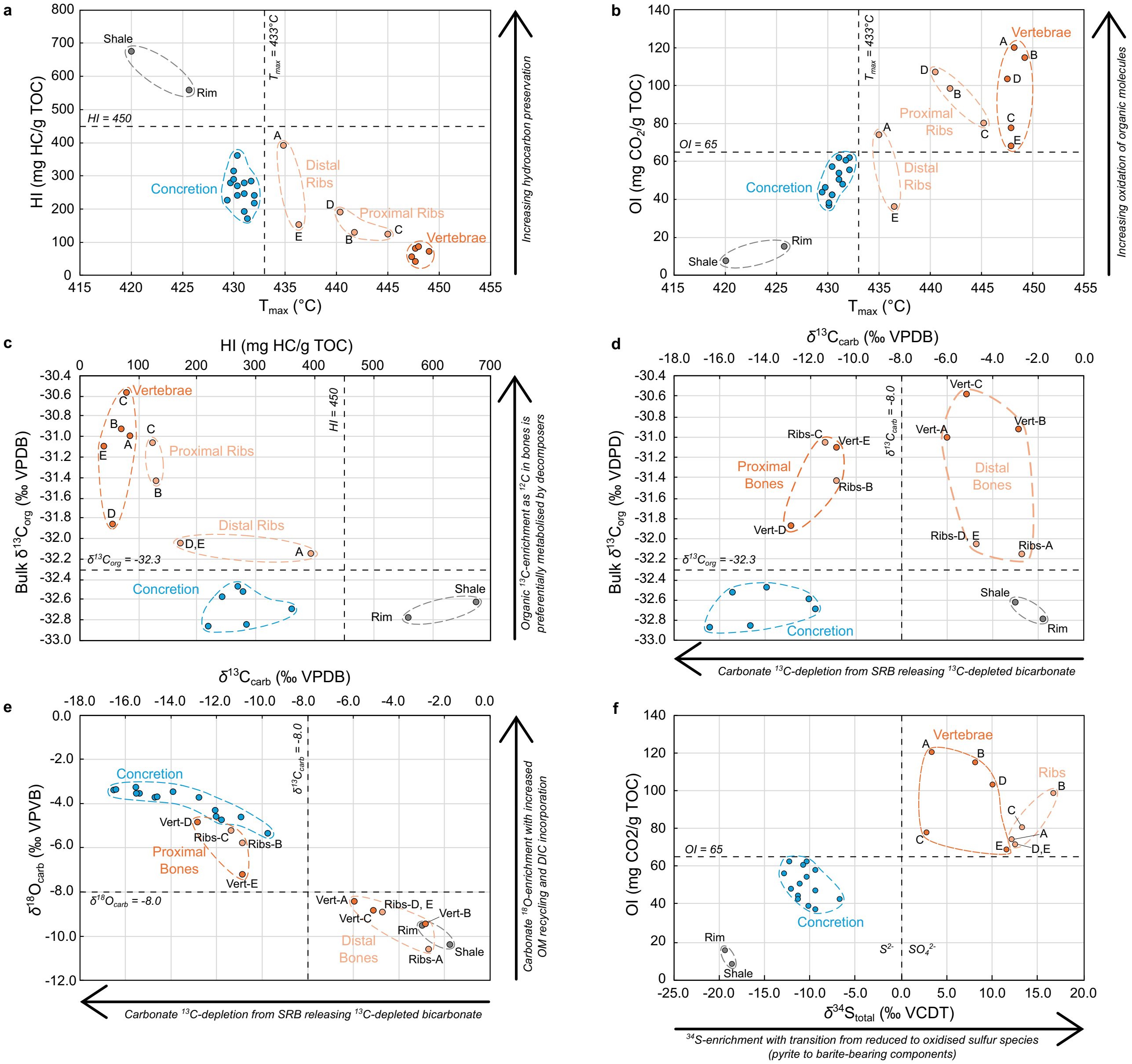

Fig. 2 | Organic matter (OM) and stable isotope characterization. Compositional differences in organic matter and carbonate due to microbial oxidation: vertebrae = orange; ribs = light orange; concretion = light blue; rim/shale = grey. **a** Binary diagram of T_{max} values (°C) against HI values (mg HC/g TOC). All concretion and bone samples exhibit HI values < 450 mg HC/g TOC, and all bones T_{max} values exceed 433 °C ($n = 26$). **b** T_{max} against OI values (mg CO_2/g TOC) ($n = 26$). All bone OI values exceed 65 mg CO_2/g TOC. **c** HI values against bulk $\delta^{13}C_{org}$ (‰ VPDB) values ($n = 17$). All bone $\delta^{13}C_{org}$ values indicate loss of ^{12}C and exceed −32.3 ‰. **d** $\delta^{13}C_{org}$ against $\delta^{13}C_{carb}$ (‰ VPDB) values ($n = 17$). Concretion and proximal bone show calcification via isotopically depleted bicarbonate yielding $\delta^{13}C_{carb} < -8.0$ ‰. **e** Plot of carbonate $\delta^{13}C_{carb}$ (‰ VPDB) against $\delta^{18}O_{carb}$ (‰ VPDB) ($n = 25$). Concretion and proximal bone $\delta^{18}O_{carb}$ values are < −8.0 ‰. **f** S $\delta^{34}S_{total}$ values plotted against OI values ($n = 25$). All bones (*i.e.*, barite-rich parts) are positively enriched in ^{34}S, concretion and shale (*i.e.*, pyrite-rich parts) are negatively depleted. Note data points Ribs-A and Ribs-E are located in the interlaminated rim and were greatly affected by secondary alteration. Full Rock Eval dataset is shown in Table 1, and stable isotopes dataset is shown in Table 2.

phosphatization of collagen (Fig. 4) required transient, slight acidity, likely caused by volatile fatty acids and H^+ ions released in the bone cavities during decomposition of ichthyosaur phospholipids[40,41]. The low HI values of the bones support the liberation of H^+ ions during OM degradation (Table 1)[10]. This acidity may have suppressed calcite precipitation while stimulating barite precipitation[42]. Barite is confined exclusively to the bone cavities (Fig. 3a–i). The barite-rich bones are resolvable in CT data since they have high density contrast against the concretion matrix (Fig. 1c; Supplementary Fig. 3). Within the vertebrae, pyrite only occurs as tiny framboids (<20 µm), which aligns with the lowest TRIS concentrations (0.04 wt. %). In the ribs, pyrite is more abundant, which agrees with a TRIS content of 0.3 wt.% (Table 2), and occurs in larger aggregates (up to 2 mm) infilling medullary canals (Supplementary Fig. 6c, d).

Barite formation required dissolved sulfate and Ba^{2+} ions (Equation 4). Given that the surrounding sediment was euxinic (*i.e.*, O_2-depleted) — as evidenced by GSB carotenoids (Supplementary Fig. 2) — sulfate must have been produced through anaerobic pathways, most likely via microbially mediated sulfur oxidation. $\delta^{34}S_{total}$ and $\delta^{34}S_{TRIS}$ values of the bones support oxidation of reduced sulfur species (Table 2)[43], potentially via disproportionation of sulfur intermediates[44–46] — a process restricted to the bone interiors.

Discussion

Microbial OM Decomposition and Concretion Formation

The geochemical signatures of the OM, mineralogy and stable isotope values in the shale, concretion, and bones are markedly distinct and spatially

Table 2 | Stable isotope and elemental data

Sample	$\delta^{13}C_{Organic}$ (‰ VPDB)	TIC (% wt.)	$\delta^{13}C_{Carbonate}$ (‰ VPDB)	$\delta^{18}O_{Carbonate}$ (‰ VPDB)	S_{Total} (% wt.)	TRIS (% wt.)	$S_{Sulfate}$ (% wt.)	$\delta^{34}S_{Total}$ (‰ VCDT)	$\delta^{34}S_{TRIS}$ (‰ VCDT)	$\delta^{34}S_{Sulfate}$ (‰ VCDT)	N_{Total} (% wt.)	$\delta^{15}N_{Total}$ (‰ air)
Vert-A	−31.0 (±0.09)	10.2	−6.0 (± 0.09)	−8.4 (± 0.03)	0.4	-	-	3.5	-	-	-	-
Vert-B	−30.9 (± 0.13)	10.3	−2.9 (± 0.04)	−9.4 (± 0.02)	0.3	-	-	8.3	-	-	-	-
Vert-C	−30.6 (± 0.05)	10.5	−5.2 (± 0.03)	−8.8 (± 0.03)	0.7	-	-	2.8	-	-	-	-
Vert-D	−31.9 (± 0.04)	9.4	−12.9 (± 0.03)	−4.8 (± 0.02)	1.7	0.04	1.7	10.2	−6.4	10.6	-	2.7
Vert-E	−31.1 (± 0.14)	8.0	−10.9 (± 0.04)	−7.2 (± 0.02)	3.4	0.03	3.4	11.9	−8.1	12.1	0.04	4.1
Vert $\bar{x}$ ($n = 5$)	−31.1 (± 0.5)	9.7	−7.6 (± 4.2)	−7.7 (± 1.8)	1.3	0.04	2.5***	7.3 (± 4.0)	−7.3 (± 1.2)	11.4 (± 1.0)	0.04	3.4 (± 1.0)
Ribs-A	−32.2 (± 0.19)	2.7	−2.7 (± 0.04)	−10.6 (± 0.04)	7.7	0.4	7.3	12.3	−14.2	13.8	0.36	2.1
Ribs-B	−31.4 (± 0.19)	2.1	−10.9 (± 0.03)	−5.8 (± 0.03)	15.6	0.2	15.4	16.8	−9.0	17.1	-	-
Ribs-C	−31.1 (± 0.22)	3.1	−11.4 (± 0.02)	−5.2 (± 0.02)	9.0	0.2	8.8	13.4	−8.6	13.9	-	-
Ribs-D, E	−32.1 (± 0.08)	4.9	−4.8 (± 0.03)	−8.9 (± 0.04)	8.9	0.3	8.6	12.6	−9.6	13.3	0.03	3.7
Ribs $\bar{x}$ ($n = 4$)	−31.7 (± 0.5)	3.2	−7.4 (± 4.4)	−7.6 (± 2.6)	10.3	0.3	10.0***	13.8 (± 2.0)	−10.3 (± 2.6)	14.5 (± 1.8)	0.19	2.9 (± 1.1)
Conc1-A	−32.5 (± 0.08)	11.0	−15.4 (± 0.06)	−3.5 (± 0.03)	4.0	2.2	1.8	−10.2	−10.3	- **	0.04	3.5
Conc1-B	-	11.7	−15.5 (± 0.05)	−3.5 (± 0.03)	3.1	2.8	0.3	−10.3	−10.8	- **	-	-
Conc2-A	-	10.4	−12.1 (± 0.05)	−4.3 (± 0.02)	5.6	6.8	−1.1*	−11.1	−9.5	- **	-	-
Conc2-B	−32.5 (± 0.11)	10.6	−13.9 (± 0.04)	−3.4 (± 0.04)	4.4	5.2	−0.8*	−9.2	−9.8	- **	0.04	5.7
Conc2-C	-	10.7	−14.7 (± 0.03)	−3.7 (± 0.04)	3.6	2.1	1.5	−11.0	−9.8	- **	0.04	5.4
Conc3-A	-	11.7	−16.5 (± 0.04)	−3.4 (± 0.02)	1.7	1.3	0.5	−11.9	−10.3	- **	0.04	4.3
Conc3-B	−32.9 (± 0.09)	11.4	−16.4 (± 0.04)	−3.3 (± 0.01)	3.3	1.5	1.9	−12.2	−10.3	- **	0.04	5.0
Conc4-A	-	10.2	−10.9 (± 0.02)	−4.6 (± 0.02)	6.4	5.5	0.8	−9.2	−9.5	- **	0.05	4.9
Conc4-B	-	10.5	−9.8 (± 0.04)	−5.3 (± 0.02)	5.6	5.4	0.3	−9.2	−9.3	- **	0.04	5.2
Conc4-C	−32.9 (± 0.02)	11.3	−14.6 (± 0.05)	−3.7 (± 0.04)	3.3	-	-	−10.7	-	-	0.04	5.4
Conc5-A	-	10.0	−12.8 (± 0.07)	−3.7 (± 0.02)	6.6	-	-	−10.1	-	-	0.04	4.0
Conc5-B	−32.7 (± 0.07)	10.9	−11.8 (± 0.04)	−4.7 (± 0.02)	2.6	-	-	−11.2	-	-	0.05	4.3
Conc5-C	-	12.1	−15.6 (± 0.02)	−3.2 (± 0.03)	1.3	-	-	−12.7	-	-	-	-
Conc6	−32.6 (± 0.05)	10.7	−12.1 (± 0.05)	−4.6 (± 0.03)	6.8	4.3	2.5	−6.6	−9.6	-	-	-
Conc $\bar{x}$ ($n = 14$)	−32.7 (± 0.2)	10.9	−13.7 (± 2.1)	−3.9 (± 0.6)	4.2	3.7	0.8***	−10.4 (± 1.5)	−9.9 (± 0.5)	-	0.04	4.8 (± 0.7)
Rim	−32.8 (± 0.05)	7.5	−1.8 (± 0.05)	−10.4 (± 0.02)	1.4	1.4	0.0****	−19.2	−19.2****	-	0.12	4.8
Shale	−32.6 (± 0.06)	3.2	−3.0 (± 0.04)	−9.5 (± 0.03)	7.8	7.8	0.0****	−18.3	−18.3****	-	0.30	2.5
Rim/Shale $\bar{x}$ ($n = 2$)	−32.7 (± 0.1)	5.4	−2.4 (± 0.9)	−9.9 (± 0.6)	4.6	4.6	0.0****	−18.8 (± 0.6)	−18.8 (± 0.6)****	-	0.2	3.7 (± 1.6)

*Calculated TRIS weight % exceeds TS weight % due to high concentration of TRIS component.**$\delta^{34}S_{TRIS}$ and $\delta^{34}S_{total}$ are too close or $\delta^{34}S$ total is lighter than $\delta^{34}S_{TRIS}$ preventing calculation of $\delta^{34}S_{Sulfate}$. ***Average $S_{sulfate}$ wt. % values calculated by averaging available $S_{sulfate}$ wt. % values per lithology/component, hence apparent average $S_{sulfate}$ wt. % can exceed average S_{Total} wt. %.

****Due to euxinic conditions in the sediment, oxidized sulfur species (sulfate) are assumed to be absent and all sulfur occurs in sulfidic form (TRIS). The $\delta^{34}S$ composition of total sulfur is then equivalent to that of TRIS.

Isotope values indicated for each sample represent the average of triplicate runs. Standard deviation for triplicate runs is indicated in brackets. Component averages ($\bar{x}$) and sample sizes indicated. The standard deviation values for component averages represent the standard deviation of all component data values. Approximated sulfate $\delta^{34}S$ (‰ VCDT) is calculated with Equation 7.

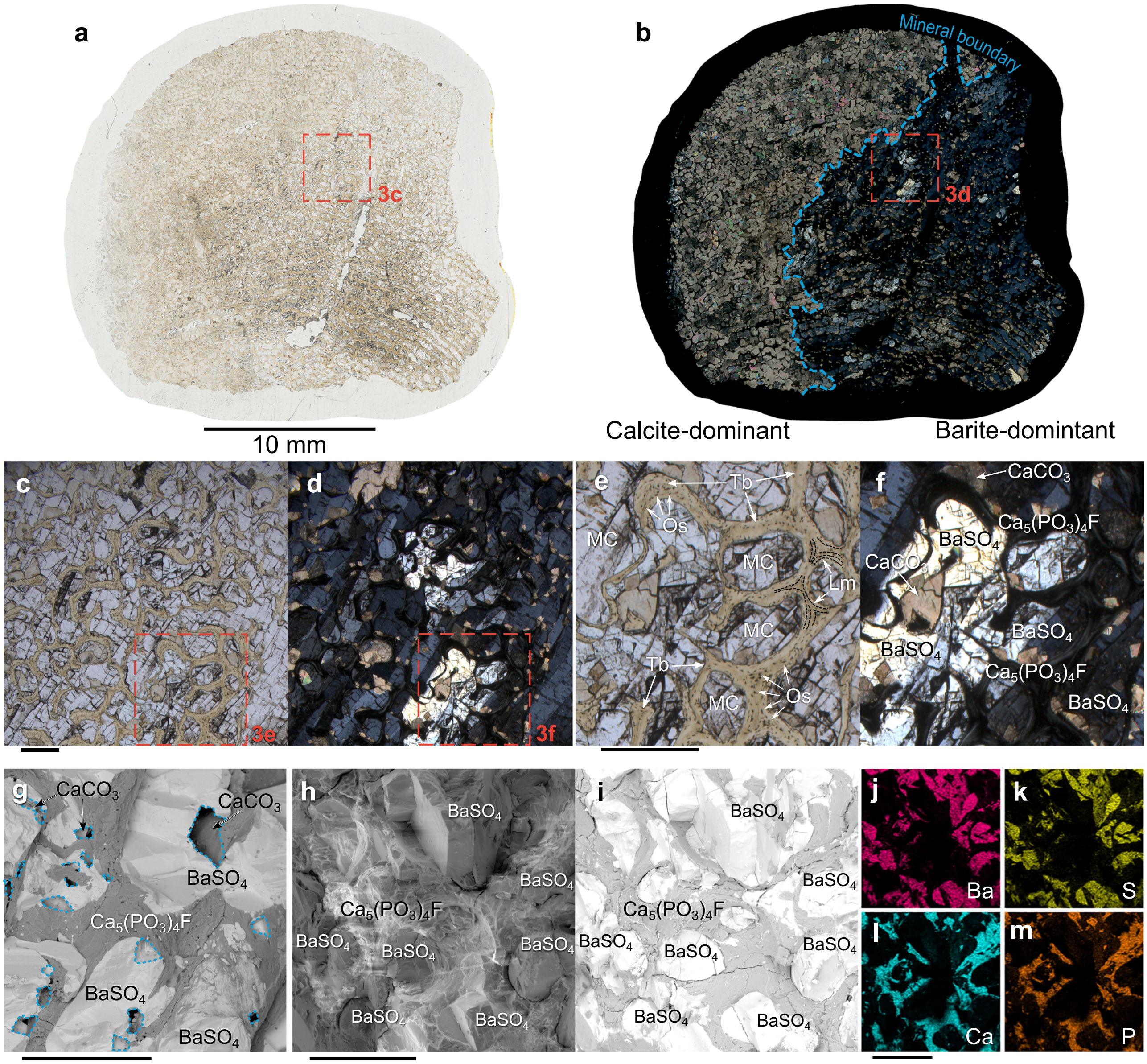

Fig. 3 | Microscopic mineralogy in ichthyosaur vertebra. **a** Thin section map of 25 mm cored vertebra sample Vert-E under plain polarized light (PPL). The thin section was sliced through the transverse plane of the vertebra. **b** Map **a** under cross polarized light (XPL). A mineral boundary (blue dashed line) between calcite infilling peripheral cavities and barite filling the interior cavities. Scale bar for **a**, **b** 10 mm. **c**, Micrograph of spongy bone trabeculae and marrow cavities under PPL. **d** Same view of **c** under XPL. **e** Inset of **c**. Tb = trabeculae, MC = marrow cavities, Lm = lamellae (black dashed lines), Os = osteocytes (dark spots). **f** Inset of **d** with identified minerals. Barite = $BaSO_4$, calcite = $CaCO_3$, fluorapatite = $Ca_5(PO_3)_4F$. **g** Backscatter electron (BSE) micrograph of Vert-B with identified minerals. Voids marked in blue dotted lines were calcite crystals dissolved during acid treatment. **h** Secondary electron (SE) micrograph of Vert-D. **i**, BSE view of **h**. Energy Dispersive X-ray Spectroscopy (EDS) maps of view (**h**, **i**), for **j** barium, **k** sulfur, **l** calcium and **m** phosphorous. **j** and **k** indicate barite in marrow cavities, **l**, **m** indicate fluorapatite composing trabeculae. Scale bar for **c**–**m** 500 µm. Larger thin-section maps are shown in Supplementary Fig. 6a, b.

separated. This pattern reflects a sequence of diagenetic processes governed by sharp spatial or temporal inter-chemical gradients.

The host shale accumulated OM from photoautotrophic planktonic debris under strongly reducing conditions driven by intense bacterial sulfate reduction[21,23,24,27]. The OM sustained microbial communities that degraded this biomass under sulfidic conditions[21], producing abundant bicarbonate as a metabolic by-product (Equations 1, 2)[14]. The bicarbonate reacted with porewater Ca^{2+}, precipitating the micritic calcite concretion around an available nucleus (Equation 3)[30]. The ^{13}C-depleted and ^{18}O-enriched cement isolated the interior bones from porewater exchange[35]. Posidonia Shale concretions likely grew within weeks to months, based on Yoshida et al.'s (2018) study of analogous carbonate concretions[47]. Higher T_{max} and OI values, but lower HI values in the concretion samples relative to the shale, indicate that SRB recycled OM from the ichthyosaur carcass and sediment. Slightly older Pliensbachian concretions from Buttenheim (Bavaria, Germany) similarly contain a mixture of OM signals of the original sediment and diagenetic transformation[48]. The Pliensbachian concretions are hypothesized to have formed at shallow burial depths and formed around local lipid-rich OM accumulations that sustained sedimentary microorganisms[48]. The ichthyosaur body would have provided an abundant source of OM metabolized by the benthic microbiome, including SRB.

Intensive microbial activity occurred within the ichthyosaur bones during soft tissue degradation, particularly in vertebrae proximal to the concretion nucleus. These show the greatest microbial OM consumption by increased T_{max}, OI, and heavier bulk $\delta^{13}C_{org}$ values in proximal bones (Fig. 2a–d). The vertebrae and rib heads were richest in consumable bone

Fig. 4 | SEM micrographs of fossilized cellular features in a vertebra. a–c SEM micrographs of mineralized collagen fibers lining the trabeculae in Vert-B. Collagen fibers were mineralized as fluorapatite. **d** 5 μm concave disc shaped cellular feature bearing resemblance to 'red blood cell-like structures' reported by Plet et al. (2017)[31] embedded in collagen fibers. The feature is composed of fluorapatite. Phosphatic preservation of these cellular features required slight acidity during decomposition. This would have initially suppressed calcite precipitation but allowed barite mineralization. Scale for each subfigure is indicated under scale bar.

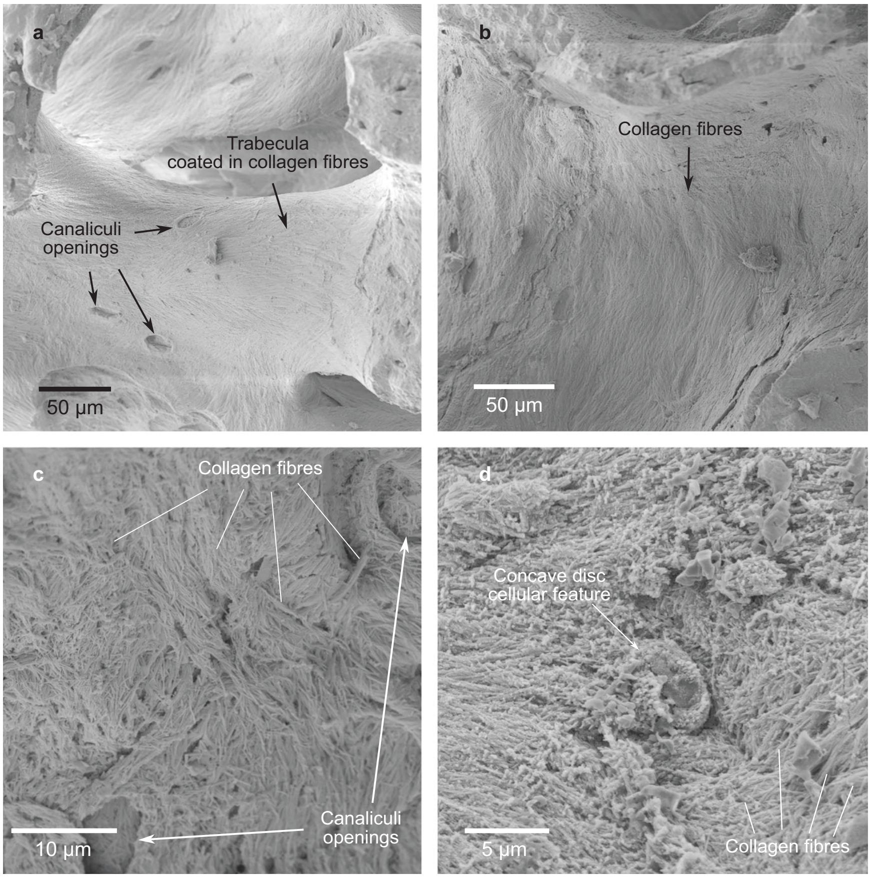

marrow proteins and lipids, including cholesterol[31]. The selective microbial utilization of labile bone lipids and their relatively heavy $\delta^{34}S_{TRIS}$ values (Supplementary Fig. 8b) indicate intensive SRB activity and enhanced H_2S fluxes within the bones. Upon lipid decomposition, volatile fatty acids were released, phosphatizing collagen fibers within the vertebrae (Fig. 4) and preventing calcitic remineralisation of the bones. Microbial activity within the ribs decreased radially towards the concretion exterior, resulting in better OM preservation in distal rib sections, as evidenced by declining T_{max} and OI values (Fig. 2a, b). Comparable microbial oxidation of fossil-associated OM has recently been reported in pterosaur bones from the Lower Cretaceous Romualdo Formation (Brazil)[11] and fish fossils from the Eocene Green River Formation (USA)[10].

The $\delta^{13}C_{carb}$ and $\delta^{18}O_{carb}$ values of calcite infilling posterior vertebrae (Vert-D, E) and proximal ribs (Fig. 2d, e) indicate derivation from the same ^{13}C-depleted bicarbonate-bearing fluid as the concretion (*i.e.*, SRB-derived precipitation), whereas anterior vertebrae (Vert-A–C) and distal ribs (Ribs-A, D, E) were infilled with authigenic calcite formed under elevated palaeotemperatures or reduced salinity due to freshwater influence (Fig. 2d, e). This demonstrates a spatiotemporal variation in chemical gradients, reflecting outwardly progressive nucleation of the concretion from the vertebral column to the distal ribs.

Barite authigenesis and microbially-mediated sulfur oxidation under anoxia

After intraosseous soft tissues were decomposed, the bone cavities were initially infilled with barite when Ba^{2+} and sulfate were abundant (Fig. 3a, b). Dissolved Ba^{2+} was likely supplied by terrestrial weathering and fluvial input[49], after biological pre-concentration into phytoplankton that settled as seafloor debris[50]. Marine bacteria are known to mediate barite biomineralisation within their cell membranes[50,51]. Intertrabecular spaces were infilled with barite while Ba^{2+} flux and supersaturation were maintained (Equation 4).

Authigenic barite in the Posidonia Shale has only been reported on fossils, typically forming mineral crusts on fish, crustaceans, coleoids, and jet[12,30]. Plet et al. (2017)[31] documented barite infilling the vertebra in another concretion-encased ichthyosaur specimen from coeval strata at Dormettingen. This pattern indicates that authigenic barite mineralization was associated with the fossilization of macro-organisms, not environmental sulfate availability, and was restricted to these oxidizing microniches within an otherwise euxinic environment. Barite is also observed in Green River Formation fish fossils[10], suggesting mineralization under temporarily acidic and oxidizing microenvironments. We propose that the ichthyosaur bones functioned as microbially active hotspots, where concentrated labile OM derived from the tissues of the ichthyosaur created a chemically dynamic microenvironment.

Recent interpretations attributed oxidation in Posidonia Shale fossils to episodic water-column ventilation[12,52–54]. However, biomarker evidence supports persistent PZE during the *exaratum* Subzone[21–23] and organic petrology indicates low energy, fine lamination, anoxic deposition leading to high OM-preservation, and abundant framboidal pyrite[55]. Carotenoids in the bones, concretion and shale (Supplementary Fig. 2) provide strong evidence for GSB, indicative of a stratified water column and PZE during the burial and concretion entombment of the ichthyosaur[21–23]. This means sulfur oxidation within the ichthyosaur was entirely anaerobic. Sulfate minerals only occur within fossils (Fig. 3; Supplementary Fig. 6)[12] and are absent in the concretion matrix (Supplementary Fig. 6, 7) and shale, implying microbially-mediated sulfur oxidation exclusively within the bones.

We hypothesize there were anaerobic metabolic pathways for sulfur-cycling bacteria to oxidize sulfide to sulfate[56]. The correlation between total S concentration and ^{34}S-enrichment (Supplementary Fig. 8a) and the relatively $^{34}S_{TRIS}$-enriched bones and concretion (Supplementary Fig. 8b) support the interpretation of microbial sulfur cycling. The approximate $\delta^{34}S_{sulfate}$ of the bones was highly enriched (Table 2), which corresponds to

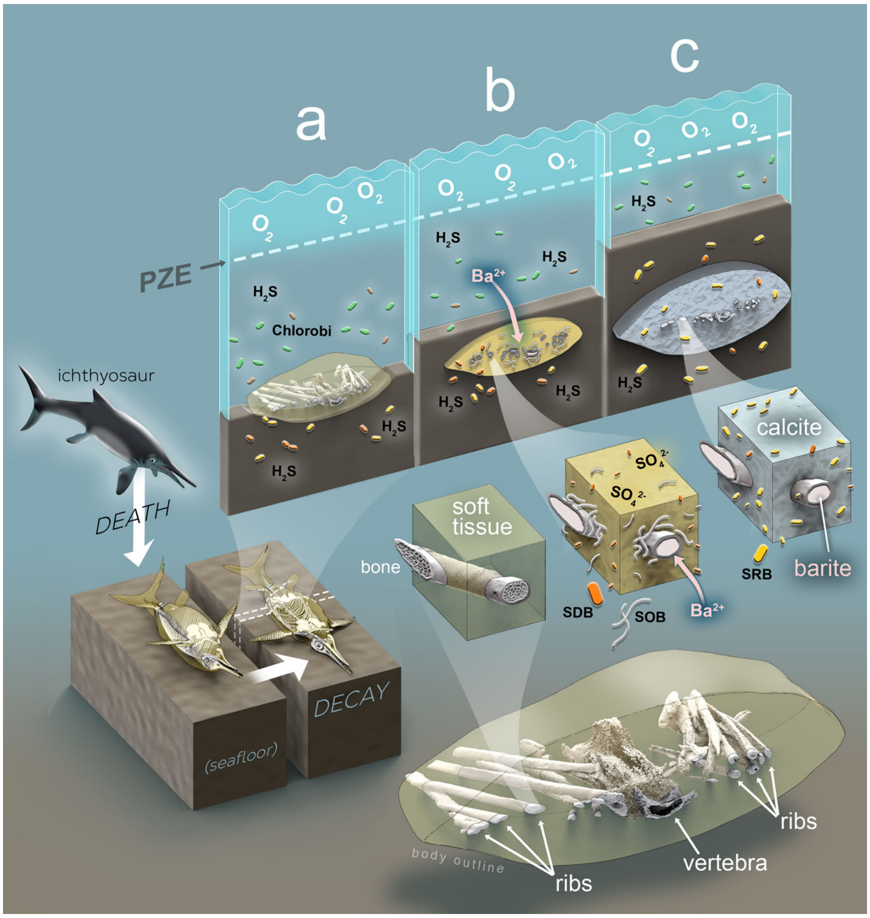

Fig. 5 | Conceptual summary of fossilization sequence. Conceptual summary of taphonomic stages leading to the preservation of the ichthyosaur specimen within a concretion under PZE. **a** Deposition of the ichthyosaur carcass at the seafloor and sinking into substrate. Bottom-waters and sediment are euxinic (H_2S-rich, O_2-depleted). **b** Soft tissues are decomposed by SRB and other microbial decomposers. Acidity briefly increased, suppressing calcite precipitation within bones. SOB and/or SDB oxidized H_2S and sulfur intermediates to SO_4^{2-}. SOB absorbed Ba^{2+} from the sediment to precipitate barite ($BaSO_4$) within the vertebrae and ribs. **c** After Ba^{2+} was exhausted or acidity neutralized, SRB released ^{13}C-depleted biocarbonate (HCO_3^-). The bicarbonate reacted with porewater Ca^{2+} and precipitated as micritic calcite ($CaCO_3$), forming the concretion. Artwork courtesy of Victor Leshyk, reproduced with permission.

isotopic fractionation via metabolic oxidation of already $^{34}S_{TRIS}$-enriched sulfide[36,37]. A microbial consortium of sulfur-oxidizing bacteria (SOB), and potentially sulfur-disproportionating bacteria (SDB), coexisted with SRB in the substrate and most likely produced the dissolved sulfate within the bone interiors[56]. Comparable SOB abundances are known from modern euxinic systems such as the Black Sea[56]. SOB has also been experimentally demonstrated to precipitate barite under dysoxia[57]. SOB and SDB are chemolithoautotrophs that metabolized inorganic carbon, unlike SRB[58].

Under anaerobic conditions, SOB can only partially oxidize sulfide to sulfur intermediates (e.g., S°, $S_2O_3^{2-}$, SO_3^{2-}, polysulfides) (Equation 5)[59]. However, SDB can oxidize sulfur intermediates to sulfate supported by Fe^{2+} and Mn^{2+} compounds, theoretically completing the full oxidation of sulfide to sulfate (Equation 6)[60,61], albeit SOB and SDB interactions in modern ecosystems are not yet fully understood[56]. Consequently, the exact anaerobic sulfur oxidation pathways that ultimately produced sulfate within the ichthyosaur bones during the Toarcian are hypothesized here only.

Taphonomic sequence

We hypothesize that fossilization of the ichthyosaur specimen included three major taphonomic stages. The first phase began after the death of the ichthyosaur. The carcass settled onto the sulfidic seafloor, quickly sank into soft substrate, and was shallowly buried (~0.1–1 m into seafloor) (Fig. 5a)[20,21,48,62].

The second major phase was the decomposition of soft tissues (Fig. 5b). SRB, SOB and SDB all co-existed syntrophically in the seabed during microbial colonization of the carcass[56,58]. During soft tissue decay, volatile fatty acids and H^+ ions were released that lowered pH, suppressed calcite precipitation from SRB activity, and promoted collagen phosphatization (Fig. 4)[41]. Sulfate production from SOB and/or SDB co-occurred with the acidic suppression of calcite precipitation. SOB and other marine bacteria incorporated Ba^{2+} into their membranes[50,51,57], supersaturating the bone cavities with both Ba^{2+} and SO_4^{2-}, thus precipitating the highly ^{34}S-enriched barite within vertebral and rib interiors until Ba^{2+} was exhausted from the sediment or acidity was neutralized. OM-metabolizing microbes, including SRB, consumed most bone-bound OM, retaining only the most recalcitrant, oxidized residues.

After soft tissue degradation, the final major stage of fossilization was precipitation of the concretion around the carcass when microbially produced bicarbonate reacted with dissolved calcium ions to form micritic calcite (Fig. 5c; Supplementary Fig. 7). Concretion growth began while sediment was uncompacted, preserving soft sediment lamination (Fig. 1a). SRB metabolized OM from biomass, increasing pH and inducing carbonate precipitation within days to weeks post-burial[30,47,63]. The concretion began nucleation around the central vertebral column and rib heads, occluding them with ^{13}C-depleted, ^{18}O-enriched calcite. The concretion radially nucleated to then encapsulate the rib midsections, as progressive burial loading above the skeleton continued. Calcite occluded any remaining bone cavities unoccupied by barite, along with pyrite in the ribs (Supplementary Fig. 6). Barite and calcite stabilized the internal structure of the concretion-surrounded bones, preventing compactional deformation. The distal ribs were initially less cemented during burial and were plastically deformed prior to their encapsulation within the concretion rim (Fig. 1a, b). The impermeable cement of the concretion shielded the bones from subsequent diagenetic alteration and enabled their exceptional 3D preservation.

These coupled microbial and mineral processes explain the spatially restricted occurrence of barite within bones, the isotopic composition of the bones, concretion and shale, and their final entombment within a carbonate concretion. This ichthyosaur specimen demonstrates that in Early Jurassic anoxic marine ecosystems, microbially mediated sulfur redox processes and biogeochemical microenvironments played a complex role in *Konservat-Lagerstätte* preservation.

Methods

Sample excavation and preparation

The sample was excavated from the Dormettingen Ölschieferbruch (oil shale quarry) by the Dotternhausen Holcim Werkforum and Fossil Museum (FWD). The specimen was donated to L. Schwark and transported to CAU Kiel. The concretion was cut into three sections, with the anatomically anterior-most section destructively analyzed in this study (Supplementary Fig. 3).

The sample was medical CT scanned at CSIRO Kensington (Australian Resources Research Centre), enabling digital 3D models to be made of the ichthyosaur bones and its host concretion in Dragonfly prior to it being destructively sampled. The sample was polished on a Vibra Lap to remove saw blade marks for photography. The specimen was drilled with a 25 mm core head to remove six horizontal core plugs and one vertical core plug (Supplementary Fig. 4). During drilling, the sample fractured along calcite veins, which exposed part of the vertebral column. The concretion was manually split and sawed with a handheld rotatory Dremel tool equipped with a pre-cleaned diamond blade to cut out rib and vertebra samples. Each horizontal core plug was cut by a Dremel blade or split by chisel into three to four pieces, separating bone components from the concretion matrix (Supplementary Fig. 5). Each sample was crushed to fine powder with a mortar and pestle or a Rocklabs Benchtop Ring Mill. A clean mortar and pestle were used for one sample each, and the Ring Mill was twice cleaned with DCM and quartz sand in between milling samples to minimize cross-contamination.

Powdered samples were extracted with a solution of 9:1 vol/vol DCM and MeOH (30 mL) using a Milestone Ethos X Advanced microwave extraction unit, using two cycles of heating to 110 °C over 15 min, 10 min static time, and 30 min cooling time, changing the solvent between cycles. The soluble extracts were decanted and collected separately, and the residue powders were dried before they were collected and weighed.

HAWK Programmed Pyrolysis (Rock Eval)

Total organic carbon (TOC) analysis and programmed pyrolysis were performed on all extracted samples. Programmed pyrolysis provides multiple parameters for OM characterization[64]. This encompasses: hydrogen indices (HI) (hydrocarbons generated from the kerogen, relative to total organic content (TOC) and expressed as mg HC/g TOC), oxygen indices (OI) (quantity of CO_2 generated from the kerogen relative to TOC and expressed as mg CO_2/g TOC), S1 (quantity of free hydrocarbons expressed as mg HC/g of rock), S2 (hydrocarbon generative potential expressed as mg HC/g of rock); T_{max} (temperature of maximum pyrolysate yield expressed in °C), and TOC amount of OM expressed in weight % and carbonate carbon expressed in weight % (Table 1). Programmed pyrolysis was undertaken with a Wildcat Technologies Hydrocarbon Analyzer workstation (HAWK®) following standard protocol[65].

Silica Gel Chromatography

Carotenoid biomarkers are contained within the aromatic fraction of the soluble extracts. Total extracts were fractionated via liquid chromatography on activated silica gel (160 °C overnight, 5.5 cm, 0.5 cm i.d.). Saturated compounds were eluted with *n*-hexane (4 mL), aromatic compounds with *n*-hexane and DCM (7:3 vol/vol, 4 mL), and polar compounds with DCM and MeOH (1:1 vol/vol, 4 mL). The aromatic fractions were evaporated to dryness, weighed and dissolved in *n*-hexane to 5 mg/mL for GC-MRM-MS analysis.

Gas chromatography–multiple reaction monitoring–mass spectrometry (GC–MRM–MS)

Aromatic fractions were analyzed by multiple reaction monitoring (MRM) using an Agilent 7890 A GC coupled to an Agilent 7000 A triple quadrupole mass spectrometer. The GC was equipped with an Agilent DB-5MS ultra-inert column (60 m, 0.25 mm i.d., 0.25 μm film thickness). A 1 μL sample was injected into a split/splitless inlet operating in pulsed splitless mode (inlet temperature 300 °C, 1.5 mL/min helium [He] carrier gas flow). The GC oven was ramped from 60 °C (2 min hold) to 220 °C at 8 °C/min (no hold), followed by a ramp to 320 °C at 2 °C/min (28 min hold). The ion source temperature was 300 °C. Data were processed using Agilent MassHunter software. Ions monitored for carotenoids at $M^+ \rightarrow 134.1$. Specific ions were selected for chlorobactane (554.5 → 134.1), β-isorenieratane (552.5 → 134.1), isorenieratane (546.5 → 134.1).

Thin section preparation

Thin sections were prepared from vertebra and rib pieces at Microanalysis Australia. The bones were subsampled using a diamond microsaw and distilled water lubrication at a minimal RPM to reduce heating and chipping. The saw blade and cutting table were cleaned thoroughly between samples to remove contaminants and debris. The cutting surfaces of the saw blades were conditioned using a pure quartz sand conditioning block to ensure no embedded material remained prior to secondary cleaning with deionised water. Cut thin-section blocks were air-dried at ambient temperature in a desiccation jar. This approach ensured minimal contamination across samples. The face of each prepared block was polished to an approximately 1200-grit flat surface to produce a suitable thin section billet and mounted to a frosted glass microscope slide with RenLam epoxy resin and hardener. Thin section billets were cured to the glass slides in a spring-activated mounting fixture for 24 hours. Using a vacuum jig, the glass-mounted billets were trimmed of excess material using a diamond trim saw lubricated with deionised water. Billet trimming yields a billet thickness of ~500–1000 μm. The saw blade and cutting table were cleaned thoroughly between samples to remove contaminants and debris. Automated lapping wheels with abrasive slurry feeds remove excess material from the trimmed billet to a thickness of slightly over 30 μm. Sample specimen holding fixtures and vacuum jigs were utilized to ensure the production of a ground-finished thin section with even thickness. The final thinning of the thin section to 30 μm and production of a polished surface was completed with three- and one-micron polishing cloths.

Acid treatment of bones

Pieces of bone were placed in three different petri dishes containing various acids (20 mL) for 24 hours. Acids used were light acetic acid (7 %), dilute HCl (0.05 M), and acetate buffer (pH 3.8). The samples were carefully washed with double-distilled water, methanol, and dichloromethane and dried with an N_2 purge. Samples were coated with platinum for SEM.

Scanning Electron Microscopy (SEM)

Microscopic observations and elemental composition analyses were conducted using scanning electron microscopy (SEM) and X-ray energy-dispersive spectroscopy (EDS) on a Tescan Mira3 VP-FESEM instrument. To prevent charging and enhance the secondary electron signal, samples were coated with a 5 nm layer of platinum. SEM imaging was performed at acceleration voltages of 5 kV and 10 kV, while EDS analyses were conducted at 20 keV with a working distance of 20 mm for 100–120 seconds.

Bulk $\delta^{13}C$ and $\delta^{15}N$ of organic matter

Aliquots of powdered and extracted sample were stirred with HCl (1 M) until bubbling ceased, then left overnight to remove all carbonates, washed with Milli-Q water, and freeze-dried. Decarbonated powder was weighed in triplicate into tin cups (Elemtex) and analyzed for bulk $\delta^{13}C$ and $\delta^{15}N$ using a Thermo Scientific Flash 2000 HT Elemental Analyzer (EA) coupled to a Thermo Delta V Advantage via a Conflo IV interface. Samples were combusted to CO_2 and N_2 in the Flash 2000 HT combustion furnace (chromium oxide, reduced copper, silvered cobaltous-cobaltic oxide) at 1020 °C. The irMS measured the ions at *m/z* 44, 45, and 46 for $\delta^{13}C$, and *m/z* 28 and 29 for $\delta^{15}N$. Isotope ratios were calculated by Thermo Isodat software and normalized to the Vienna Pee

Dee Belemnite (VPDB) carbon isotope scale using the standard reference materials NBS-19 ($\delta^{13}C + 1.95$ ‰) and L-SVEC ($\delta^{13}C$ −46.6 ‰), and the atmospheric nitrogen (air) scale using the standard reference materials USGS40 ($\delta^{15}N$ −4.52 ‰) and USGS41a ($\delta^{15}N + 47.55$ ‰). Measurement accuracy was assessed using the standard reference material IAEA-600 ($\delta^{13}C$ −27.77 ‰, $\delta^{15}N + 1.00$ ‰).

$\delta^{34}S$ of total sulfur and total reduced inorganic sulfur (TRIS)

For measuring contents and the stable isotope composition of total S, dried and homogenized samples were weighed in pre-cleaned tin cups and combusted in a Thermo Scientific Flash EA Isolink Elemental Analyzer connected to a Thermo Finnigan MAT 253 gas mass spectrometer via a Thermo Conflo IV split interface[66]. The results are given in the conventional δ-notation, where the given results in [‰] are equivalent to [mUr] (milliUrey). Sample gas was transported in a stream of high-grade (5.0) helium. International isotope intercomparison materials were used to convert the isotope ratios to the Vienna-Canyon Diablo Troilite (VCDT) scales with a precision of better than ± 0.3 ‰ ($\delta^{34}S$).

The TRIS (total reducible sulfur) content was extracted via the reaction with hot acidic Cr(II)Cl_2 solution[67,68] and the developed H_2S was trapped quantitatively as ZnS. The homogenized suspension was measured spectrophotometrically with a Specord 40 spectrophotometer following Cline (1969)[69]. Afterwards, the ZnS was transferred to Ag_2S for further stable isotope analysis.

$\delta^{13}C$ and $\delta^{18}O$ of carbonate

$\delta^{13}C$ and $\delta^{18}O$ values of the carbonate fraction were measured on CO_2 liberated by the reaction with H_3PO_4 at 72 °C with a precision of better than ± 0.15 ‰[70]. Reaction took place in a Thermo Gasbench II connected to a Thermo Finnigan MAT 253 gas mass spectrometer via a Thermo Conflo IV spilt interface. Scaling of measured carbon and oxygen isotope results to the VPDB scale took place via carbonate reference materials (NBS19 and LVSEC).

$$2CH_2O + SO_4^{2-}(aq) \rightarrow 2HCO_3^-(aq) + H_2S(aq) \quad (1)$$

$$2CH_2O + SO_4^{2-}(aq) \rightarrow HCO_3^-(aq) + CO_2(aq) + HS^-(aq) + H_2O \quad (2)$$

$$Ca^{2+}(aq) + 2HCO_3^-(aq) \rightarrow CaCO_3(s) + H_2O + CO_2(aq) \quad (3)$$

$$Ba^{2+}(aq) + SO_4^{2-}(aq) \rightarrow BaSO_4(s) \quad (4)$$

$$CO_2(aq) + 2H_2S(aq) \rightarrow CH_2O + H_2O + 2S^o(aq) \quad (5)$$

$$4H_2O + 4S^o(aq) \rightarrow 3H_2S(aq) + SO_4{}^{2-}(aq) + 2H^+(aq) \quad (6)$$

$$\delta^{34}S_{sulfate} = \frac{\delta^{34}S_{total} - (\%wt.S_{TRIS} \times \delta^{34}S_{TRIS})}{\%wt.S_{sulfate}}$$

Reporting summary

Further information on research design is available in the Nature Portfolio Reporting Summary linked to this article.

Data availability

Image and figure data are available under a CC BY-NC 4.0 Licence on Mendeley Data at https://doi.org/10.17632/x3bsn62g3c.3. CT and GC-MRM-MS data are not publicly available due to privacy and ethical restrictions and are only available upon request. This paper does not report original code.

Received: 28 October 2025; Accepted: 25 February 2026;
Published online: 25 March 2026

References

1. Calvert, S. E. & Pedersen, T. Organic carbon accumulation and preservation in marine sediments: how important is anoxia? Productivity, accumulation and preservation of organic matter in recent and ancient sediments 231–263 (1992).
2. Calvert, S. E., Bustin, R. M. & Ingall, E. D. Influence of water column anoxia and sediment supply on the burial and preservation of organic carbon in marine shales. *Geochim. Cosmochim* **60**, 1577–1593 (1996).
3. Canfield, D. E. Factors influencing organic carbon preservation in marine sediments. *Chem. Geol.* **114**, 315–329 (1994).
4. Allison, P. A. The role of anoxia in the decay and mineralization of proteinaceous macro-fossils. *Paleobiology* **2**, 139–154 (1988).
5. Riegel, W., Loh, M., Maul, B. & Prauss, M. Effects and causes in a black shale event-the Toarcian Posidonia Shale of NW Germany. *Glob. Bio-events Proc. 1st Meet. IGCP Proj.* **216**, 267–276 (1986).
6. Clements, T. & Gabbott, S. Exceptional Preservation of Fossil Soft Tissues. in *eLS* 1–10 (Wiley, 2022). https://doi.org/10.1002/9780470015902.a0029468.
7. Sagemann, J., Bale, S. J., Briggs, D. E. G. & Parkes, R. J. Controls on the formation of authigenic minerals in association with decaying organic matter: an experimental approach. *Geochim. Cosmochim. Acta* **63**, 1083–1095 (1999).
8. Huckriede, H. & Meischner, D. Origin and environment of manganese-rich sediments within black-shale basins. *Geochim. Cosmochim. Acta* **60**, 1399–1413 (1996).
9. Gueriau, P. et al. Oxidative conditions can lead to exceptional preservation through phosphatization. *Geology* **48**, 1164–1168 (2020).
10. Elson, A. L. et al. Fossilisation of Fish Soft Tissue in Oxidative Microniches of Anoxic Sediments. *Environ. Microbiol.* **27**, e70188 (2025).
11. Grice, K. et al. Multi-staged biomineralization and biomarker preservation in a 113-million-year-old pterosaur bone via local redox shifts in diagenesis. *iScience*, (2026).
12. Muscente, A. D. et al. What role does anoxia play in exceptional fossil preservation? Lessons from the taphonomy of the Posidonia Shale (Germany). *Earth-Sci. Re.* **238**, (2023).
13. McNamara, M. E., Orr, P. J., Alcala, L., Anadon, P. & Penalver, E. What controls the taphonomy of exceptionally preserved taxa—environment or biology? A case study using frogs from the Miocene Libros Konservat-Lagerstätte (Teruel, Spain). *PALAIOS* **27**, 63–77 (2012).
14. Raiswell, R. The microbiological formation of carbonate concretions in the Upper Lias of NE England. *Chem. Geol.* **18**, 227–244 (1976).
15. Grice, K., Holman, A. I., Plet, C. & Tripp, M. Fossilised biomolecules and biomarkers in carbonate concretions from Konservat-Lagerstätten. *Minerals* **9**, 1–15 (2019).
16. McCoy, V. E. Concretions as agents of soft-tissue preservation: a review. *Paleontol. Soc. Pap.* **20**, 147–162 (2014).
17. McCoy, V. E., Young, R. T. & Briggs, D. E. G. Factors controlling exceptional preservation in concretions. *Palaios* **30**, 272–280 (2015).
18. Allison, P. A. Konservat-Lagerstätten: cause and classification. *Paleobiology* **14**, 331–344 (1988).
19. Riegraf, W., Werner, G., Lörcher, F. & Schmitt, C. *Der Posidonienschiefer: Biostratigraphie, Fauna Und Fazies Des Südwestdeutschen Untertoarciums (Lias Espilon). Der Posidonienschiefer: Biostratigraphie, Fauna und Fazies des südwestdeutschen Unteroarciums (Lias Espilon)* (1984).
20. Röhl, H. J., Schmid-Röhl, A., Oschmann, W., Frimmel, A. & Schwark, L. The Posidonia Shale (Lower Toarcian) of SW-Germany: An oxygen-depleted ecosystem controlled by sea level and palaeoclimate. *Palaeogeogr., Palaeoclimatol., Palaeoecol.* **165**, 27–52 (2001).
21. Schwark, L. & Frimmel, A. Chemostratigraphy of the Posidonia Black Shale, SW-Germany II. Assessment of extent and persistence of

photic-zone anoxia using aryl isoprenoid distributions. *Chem. Geol.* **206**, 231–248 (2004).

22. Ajuaba, S. et al. Biomarker and compound-specific isotope records across the Toarcian CIE at the Dormettingen section in SW Germany. *Int. J. Earth Sci.* **111**, 1631–1661 (2022).
23. Schouten, S., Van Kaam-Peters, H. M. E., Rijpstra, W. I. C., Schoell, M. & Sinninghe Damste, J. S. Effects of an oceanic anoxic event on the stable carbon isotopic composition of early Toarcian carbon. *Am. J. Sci.* **300**, 1–22 (2000).
24. Moldowan, J. M., Sundararaman, P. & Schoell, M. Sensitivity of biomarker properties to depositional environment and/or source input in the Lower Toarcian of SW-Germany. *Org. Geochem.* **10**, 915–926 (1986).
25. Maxwell, E. E. New metrics to differentiate species of Stenopterygius (Reptilia: Ichthyosauria) from the Lower Jurassic of southwestern Germany. *J. Paleontol.* **86**, 105–115 (2012).
26. Maxwell, E. E. & Cortés, D. A revision of the Early Jurassic ichthyosaur Hauffiopteryx (Reptilia: Ichthyosauria), and description of a new species from southwestern Germany. *Palaeontol. Electron.* **23**, 1–43 (2020).
27. Frimmel, A., Oschmann, W. & Schwark, L. Chemostratigraphy of the Posidonia Black Shale, SW Germany I. Influence of sea-level variation on organic facies evolution. *Chem. Geol.* **206**, 199–230 (2004).
28. Röhl, H.-J. & Schmid-Röhl, A. Lower Toarcian (Upper Liassic) Black Shales of the Central European Epicontinental Basin: A Sequence Stratigraphic Case Study from the SW German Posidonia Shale. in *Deposition of Organic-Carbon-Rich Sediments: Models* 165–189 https://doi.org/10.2110/pec.05.82.0165 (2005).
29. Reinhardt, M. et al. The taphonomic fate of isorenieratene in Lower Jurassic shales—controlled by iron? *Geobiology* **16**, 237–251 (2018).
30. Plet, C. et al. Microbially-mediated fossil-bearing carbonate concretions and their significance for palaeoenvironmental reconstructions: A multi-proxy organic and inorganic geochemical appraisal. *Chem. Geol.* **426**, 95–108 (2016).
31. Plet, C. et al. Palaeobiology of red and white blood cell-like structures, collagen and cholesterol in an ichthyosaur bone. *Sci. Rep.* **7**, 13776 (2017).
32. Jäger, M. *The Museum of Fossils in the Werkforum: Guidebook of the Exhibition of Jurassic Fossils*. (Holcim (Baden-Württemberg) GmbH, Dotternhausen, 2005).
33. Martin, J. E. et al. Stenopterygiids from the lower Toarcian of Beaujolais and a chemostratigraphic context for ichthyosaur preservation during the Toarcian Oceanic Anoxic Event. *Carbon Cycle Ecosyst. Response Jenkyns Event Early Toarcian* **514**, 153–172 (2021).
34. Bonnevier Wallstedt, I. et al. Skin Anatomy, Bone Histology and Taphonomy of a Toarcian (Lower Jurassic) Ichthyosaur (Reptilia: Ichthyopterygia) from Luxembourg, with Implications for Paleobiology. *Diversity* **16**, 492 (2024).
35. Wetzel, A. & Bojanowski, M. 'Resurrected' concretions – their resumed cementation after exhumation, transport, re-deposition and exploitation by producers of the trace fossil Chondrites when still being soft. *Mar. Pet. Geol.* **182**, 107576 (2025).
36. Böttcher, M. E. Sulfur Isotope Fractionation in the Biogeochemical Sulfur Cycle of Marine Sediments. *Isotopes Environ. Health Stud.* **37**, 97–99 (2001).
37. Böttcher, M. E., Hespenheide, B., Brumsack, H.-J. & Bosselmann, K. Stable isotope biogeochemistry of the sulfur cycle in modern marine sediments: I. seasonal dynamics in a temperate intertidal sandy surface sediment. *Isotopes Environ. Health Stud.* **40**, 267–283 (2004).
38. Stüeken, E. E., Tino, C., Arp, G., Jung, D. & Lyons, T. W. Nitrogen isotope ratios trace high-pH conditions in a terrestrial Mars analog site. *Sci. Adv.* **6**, eaay3440 (2020).
39. Seal, R. R. I. I., Alpers, C. N. & Rye, R. O. Stable Isotope Systematics of Sulfate Minerals. *Rev. Mineral. Geochem.* **40**, 541–602 (2000).
40. Briggs, D. E. G., Kear, A. J., Martill, D. M. & Wilby, P. R. Phosphatization of soft-tissue in experiments and fossils. *J. -Geol.Soc.* **150**, 1035–1038 (1993).
41. Briggs, D. E. G. & Wilby, P. R. The role of the calcium carbonate-calcium phosphate switch in the mineralization of soft-bodied fossils. *J. Geol. Soc.* **153**, 665–668 (1996).
42. Ruiz-Agudo, C., Putnis, C. V., Ruiz-Agudo, E. & Putnis, A. The influence of pH on barite nucleation and growth. *Chem. Geol.* **391**, 7–18 (2015).
43. Kelly, D. P. Biochemistry of the chemolithotrophic oxidation of inorganic sulphur. *Philos. Trans. R. Soc. Lond. B, Biol. Sci.* **298**, 499–528 (1997).
44. Bak, F. & Cypionka, H. A novel type of energy metabolism involving fermentation of inorganic sulphur compounds. *Nature* **326**, 891–892 (1987).
45. Canfield, D. E. & Thamdrup, B. The Production of 34S-Depleted Sulfide During Bacterial Disproportionation of Elemental Sulfur. *Science* **266**, 1973–1975 (1994).
46. Böttcher, M. E., Thamdrup, B. & Gehre, M. & Theune, A. 34S/32S and 18O/16O Fractionation During Sulfur Disproportionation by Desulfobulbus propionicus. *Geomicrobiol. J.* **22**, 219–226 (2005).
47. Yoshida, H. et al. Early post-mortem formation of carbonate concretions around tusk-shells over week-month timescales. *Sci. Rep.* **5**, 14123 (2015).
48. Thiel, V. & Hoppert, M. Fatty acids and other biomarkers in two Early Jurassic concretions and their immediate host rocks (Lias δ, Buttenheim clay pit, Bavaria, Germany). *Org. Geochem.* **120**, 42–55 (2018).
49. Brumsack, H. J. Inorganic geochemistry of the German 'Posidonia Shale': Palaeoenvironmental consequences. *Geol. Soc. Spec. Publ.* **58**, 353–362 (1991).
50. Gonzalez-Muñoz, M. T., Martinez-Ruiz, F., Morcillo, F., Martin-Ramos, J. D. & Paytan, A. Precipitation of barite by marine bacteria: A possible mechanism for marine barite formation. *Geology* **40**, 675–678 (2012).
51. Xu, T., Shang, S., Tian, H., Bei, K. & Cao, Y. Numerical Simulation on Authigenic Barite Formation in Marine Sediments. *Minerals* **9**, 98 (2019).
52. De La Garza, R. G., Sjövall, P., Hauff, R. & Lindgren, J. Preservational modes of some ichthyosaur soft tissues (Reptilia, Ichthyopterygia) from the Jurassic Posidonia Shale of Germany. *Palaeontology* **66**, 1–17 (2023).
53. Dick, D. G. An ichthyosaur carcass-fall community from the Posidonia Shale (Toarcian) of Germany. *Palaios* **30**, 353–361 (2015).
54. Maxwell, E. E. et al. Evaluating the Existence of Vertebrate Deadfall Communities from the Early Jurassic Posidonienschiefer Formation. *Geosciences* **12**, 158 (2022).
55. Littke, R., Leythaeuser, D., Rullkötter, J. & Baker, D. R. Keys to the depositional history of the Posidonia Shale (Toarcian) in the Hils Syncline, northern Germany. *SP* **58**, 311–333 (1991).
56. van Vliet, D. M. et al. The bacterial sulfur cycle in expanding dysoxic and euxinic marine waters. *Environ. Microbiol.* **23**, 2834–2857 (2021).
57. Bonny, S. M. & Jones, B. Experimental Precipitation of Barite (BaSO4) Among Streamers of Sulfur-Oxidizing Bacteria. *J. Sediment. Res.* **78**, 357–365 (2008).
58. van den Ende, F. P., Meier, J. & van Gemerden, H. Syntrophic growth of sulfate-reducing bacteria and colorless sulfur bacteria during oxygen limitation. *FEMS Microbiol Ecol.* **23**, 65–80 (1997).
59. Kuenen, J. G. Colourless sulfur bacteria and their role in the sulfur cycle. *Plant Soil* **43**, 49–76 (1975).
60. Thamdrup, B., Finster, K., Hansen, J. W. & Bak, F. Bacterial Disproportionation of Elemental Sulfur Coupled to Chemical Reduction of Iron or Manganese. *Appl. Environ. Microbiol.* **59**, 101–108 (1993).
61. Böttcher, M. E., Thamdrup, B. & Vennemann, T. W. Oxygen and sulfur isotope fractionation during anaerobic bacterial disproportionation of

elemental sulfur. *Geochim. Cosmochimica Acta* **65**, 1601–1609 (2001).

62. Martill, D. M. Soupy Substrates: A Medium for the Exceptional Preservation of Ichthyosaurs of the Posidonia Shale (Lower Jurassic) of Germany. *Darmstädter. Beitr. Age Zur. Naturgewchichte* **2**, 77–97 (1993).
63. Dhami, N. K. et al. Microbially mediated fossil concretions and their characterization by the latest methodologies: A review. *Front Microbiol.* **14**, 1225411 (2023).
64. Behar, F., Beaumont, V. & De, H. L. Technologie Rock-Eval 6: Performances et développements. *Oil Gas. Sci. Technol.* **56**, 111–134 (2001).
65. Maende, A., Pepper, A. S., Jarvie, D. M. & Weldon, W. D. Advanced pyrolysis data and interpretation methods to identify unconventional reservoir sweet spots in fluid phase saturation and fluid properties (API gravity) from drill cuttings and cores. *SearchDiscov.* **80596**, 417–452 (2017).
66. Pollmann, T., Böttcher, M. E. & Giani, L. Young soils of a temperate barrier island under the impact of formation and resetting by tides and wind. *CATENA* **202**, 105275 (2021).
67. Fossing, H. & Jørgensen, B. B. Measurement of bacterial sulfate reduction in sediments: Evaluation of a single-step chromium reduction method. *Biogeochemistry* **8**, 205–222 (1989).
68. Rooze, J. et al. Bottom-trawling signals lost in sediment: A combined biogeochemical and modeling approach to early diagenesis in a perturbed coastal area of the southern Baltic Sea. *Sci. Total Environ.* **906**, 167551 (2024).
69. Cline, J. D. Spectrophotometric determination of hydrogen sulfide in natural waters. *Limnol. Oceanogr.* **14**, 454–458 (1969).
70. Böttcher, M. E. et al. Multi-isotope (Ba, C, O) partitioning during experimental carbonatization of a hyper-alkaline solution. *Chemie der Erde* **78**, 241–247 (2018).

Acknowledgements

This research was conducted as part of a Ph.D. research project funded by an Australian Government Research Training Program Scholarship, the Australian Research Council (ARC), for an ARC Laureate Fellowship grant (FL210100103) awarded to K. Grice and a DFG Grant (SCHW554/29) awarded to L. Schwark. Part of this research was undertaken using the Tescan Mira3 VP-FESEM with Oxford Instruments X-Max 150 SDD X-ray detector and AZtec Synergy software (ARC LE130100053) at the John de Laeter Centre to perform SEM–EDS analysis. We thank Dr Annette Schmid and the Dotternhausen Holcim Werkforum and Fossil Museum for donating the research specimen. We thank Dr Lionel Esteban and Dr Mustafa Sari of CSIRO Kensington (Australian Resources Research Centre) for CT scanning the specimen, Justin Tomlinson of Core Laboratories for assisting with core plug sampling, and Dr Robert Madden of Microanalysis Australia for the preparation of thin sections and specimen polishing. We thank Peter Hopper for assisting with GC–MRM–MS analysis. We thank Victor Leshyk for illustrating the conceptual summary figure. We thank our peer reviewers for their constructive feedback on our manuscript.

Author contributions

Conceptualization: A.J.Y.J., L.S., K.G. Methodology: A.J.Y.J., L.S., S.F.P., A.I.H., L.M.B., M.D.M., M.E.B., K.G. Project administration: K.G. Supervision: K.G., L.S., S.F.P. Writing – original draft: A.J.Y.J., L.S., K.G. Writing – review and editing: A.J.Y.J., L.S., S.F.P., A.I.H., L.M.B., M.D.M., M.E.B., K.G.

Competing interests

The authors declare no competing interests.

Additional information

Supplementary information The online version contains supplementary material available at https://doi.org/10.1038/s43247-026-03366-6.

Correspondence and requests for materials should be addressed to Andrew Ji Yao Jian, Lorenz Schwark or Kliti Grice.

Peer review information *Communications Earth and Environment* thanks Zhiyong Lin, Theodore M. Present, and the other anonymous reviewer(s) for their contribution to the peer review of this work. Primary Handling Editors: Somaparna Ghosh. A peer review file is available.